Journal of Tissue Engineering
Volume 11: 1–16
© The Author(s) 2020
Article reuse guidelines:
sagepub.com/journals-permissions
DOI: 10.1177/2041731420965797
journals.sagepub.com/home/tej
SAGE

The combination of multi-functional ingredients-loaded hydrogels and three-dimensional printed porous titanium alloys for infective bone defect treatment

Shichong Qiao[1*], Dongle Wu[1*], Zuhao Li[2], Yu Zhu[1], Fei Zhan[3], Hongchang Lai[1] and Yingxin Gu[1]

Abstract

Biomaterial with the dual-functions of bone regeneration and antibacterial is a novel therapy for infective bone defects. Three-dimensional (3D)-printed porous titanium (pTi) benefits bone ingrowth, but its microporous structure conducive to bacteria reproduction. Herein, a multifunctional hydrogel was prepared from dynamic supramolecular assembly of sodium tetraborate ($Na_2B_4O_7$), polyvinyl alcohol (PVA), silver nanoparticles (AgNPs) and tetraethyl orthosilicate (TEOS), and composited with pTi as an implant system. The pTi scaffolds have ideal pore size and porosity matching with bone, while the supramolecular hydrogel endows pTi scaffolds with antibacterial and biological activity. In vitro assessments indicated the 3D composite implant was biocompatible, promoted bone marrow mesenchymal stem cells (BMSCs) proliferation and osteogenic differentiation, and inhibited bacteria, simultaneously. In vivo experiments further demonstrated that the implant showed effective antibacterial ability while promoting bone regeneration. Besides distal femur defect, the innovative scaffolds may also serve as an ideal biomaterial (e.g. dental implants) for other contaminated defects.

Keywords

Supramolecular hydrogels, antibacterial scaffolds, three-dimensional printed porous titanium alloys, bone regeneration, inorganic-organic composite

Received: 7 July 2020; accepted: 23 September 2020

Introduction

Repairing critical bone defects caused by trauma, revision arthroplasty, tumor resection, infection, and *etc.* is a great challenge in clinical practice. Under such circumstances, the regeneration ability of the bone tissue is not sufficient without effective external intervention.[1] However, there is no ideal and efficient biomaterial for bone tissue

---

[1]Department of Implant Dentistry, Shanghai Ninth People's Hospital, College of Stomatology, Shanghai Jiaotong University School of Medicine, National Clinical Research Center for Oral Diseases; Shanghai Key Laboratory of Stomatology & Shanghai Research Institute of Stomatology, Shanghai, P.R. China
[2]Department of Pain, Renji Hospital, Shanghai Jiaotong University School of Medicine, Shanghai, P. R. China
[3]Shanghai Zammax Biotech Co., Ltd. Shanghai, P.R. China

*These author contribute to this article equally.

Corresponding authors:
Hongchang Lai, Department of Implant Dentistry, Shanghai Ninth People's Hospital, College of Stomatology, Shanghai Jiaotong University School of Medicine, National Clinical Research Center for Oral Diseases; Shanghai Key Laboratory of Stomatology & Shanghai Research Institute of Stomatology, NO.639 zhizaoju Road, Shanghai, 200011, P.R. China.
Email: hongchang_lai@126.com

Yingxin Gu, Department of Implant Dentistry, Shanghai Ninth People's Hospital, College of Stomatology, Shanghai Jiaotong University School of Medicine, National Clinical Research Center for Oral Diseases; Shanghai Key Laboratory of Stomatology & Shanghai Research Institute of Stomatology, Shanghai, 200011, P.R. China.
Email: yingxingu@163.com

Creative Commons Non Commercial CC BY-NC: This article is distributed under the terms of the Creative Commons Attribution-NonCommercial 4.0 License (https://creativecommons.org/licenses/by-nc/4.0/) which permits non-commercial use, reproduction and distribution of the work without further permission provided the original work is attributed as specified on the SAGE and Open Access pages (https://us.sagepub.com/en-us/nam/open-access-at-sage).

engineering so far, especially for the repair of infected bone.[2] In the case of open fracture, the infective rates are ranging from 20% to 50%, which result in significantly prolonging hospitalization and aggravating economic burden for patients.[3] The defects area and most synthetic bone substitutes are apt to bacterial adherence and subsequent biofilm formation, thus promoting the progress of bone infection.[4,5] Therefore, alternative bioactive materials that can potentially enhance osteogenesis and inhibit bacteria are of great scientific and clinical significance.

Three-dimensional (3D) printed porous titanium alloy (pTi) can customize the implants according to the requirements of physiological anatomy and clinical treatment, so as to reconstruct the original anatomy and restore the function as much as possible.[6] Moreover, 3D printed microporous structure is of great significance for practical application. The introduction of microporous structure can decrease the mechanical parameters, such as the elastic modulus of the implant, so as to make it more compatible with the host bone tissue, thus effectively avoid stress-shielding and osteolysis.[7] Besides, this interconnected porosity increases the surface area of the prosthesis for initial stability, promotes angiogenesis and induces bone ingrowth.[8,9] Although 3D printed implants can meet the requirements of infectious bone defects for the morphology and microstructure of the repair materials, they still cannot solve the problem of infection, and the porous structure also provides an absolute place for bacterial reproduction.[10] What's more, inorganic 3D printed implants are bioinertness and lack of bioactivities for native stem cells survival, differentiation, and communication.[11,12] Therefore, biomimetic modifications are suggested to optimize the biocompatible and antibacterial properties of the 3D printed microporous surface, and rational design of biomaterial coating is a simple, efficient, and promising strategy to endow 3D printed implants surfaces with desirable bioactivity.

Hydrogels are generally fabricated by the cross-linking of hydrophilic polymer chains within an aqueous microenvironment.[13–15] These biomaterials are characterized by good biocompatibility, biodegradability, large water content, and tissue-like flexibility.[16,17] With the above advantages, hydrogels have exceptional promise in wide range of applications, such as drug-delivery vehicles, flexible device, biosensors, and matrices for tissue engineering.[16,18–21] Recently, there has been increasing interest in developing hydrogels which made from inorganic nanoparticles. In this type of hydrogel, inorganic nanoparticles are introduced into hydrogel 3D networks *via* covalent crosslink or non-covalent supramolecular interactions (e.g. hydrophobic interactions, π-π stacking, Van der Waals forces, and hydrogen bonds). As a result, this formulation hydrogel not only have advantages of traditional hydrogels, but also integrate the unique properties of nanoparticles, for instance, fluorescence,[22] adhesion,[23–26] biological activity,[27] conductivity,[28,29] as well as magnetic properties.[30] Therefore, the rational design of hydrogels with controlled physical and biological properties can be used to regulate 3D printed implants functionality.

The traditional strategy for preparing 3D printing metal antibacterial implant is to print the prosthesis firstly, and then use physical or chemical methods to coat the surface with antibacterial materials.[31,32] This traditional preparation process of the customized antibacterial metal implant is complex, time consuming, and costly, so it is difficult to be widely used in clinical. While, the antibacterial hydrogel is simple to be synthesized and can be prepared before the 3D printed metal implants and preserved for use.[33] Once the scaffold is printed, the antibacterial hydrogel can be immediately filled into the micropores to form a composition implant system for the surgery of infectious bone defects. In this study, Ti6Al4V, which has been approved and widely used in clinical practice, as the basic printing material, was used to print the framework of the scaffold to match the bone defects. The plastic antibacterial hydrogel worked as a filler to fill the microporous of the scaffold, thus a new composite implant was constructed with mechanical properties, as well as dual-functions of antibacterial and osteogenic induction, to improve the repair of infected bone (**Scheme 1**). The composite scaffold composes of 3D-printed pTi and multifunctional supramolecular hydrogels. The macroscopic morphology and microscopic structure of 3D-printed pTi meet the requirements for the infectious bone regeneration. The hydrogels are prepared from dynamic supramolecular assembly of sodium tetraborate ($Na_2B_4O_7$), polyvinyl alcohol (PVA), silver nanoparticles (AgNPs) and tetraethyl orthosilicate (TEOS). We first selected hydrogel components that were safe and compatible with biological systems, and then directly manufactured a hydrogel with a multi-network structure. In short, the $Na_2B_4O_7$ solution was added into the mixed solution of PVA, TEOS, Ag NPs, and 3D-printed pTi under vigorous stirring at 90°C. The transparent conductive supramolecular hydrogel is immediately formed on the surface of 3D-printed pTi. After introduction of multifunctional hydrogels, the 3D-printed pTi was further endowed with antibacterial ability and biological activity. The results of in vitro experiments demonstrate that the composited scaffold can promote bone marrow mesenchymal stem cells (BMSCs) proliferation and osteogenic differentiation. In addition, antibacterial analysis illustrates that this composite pTi scaffold exhibits broad antibacterial activity against *Staphylococcus aureus* (*S. aureus*), *methicillin-resistant S. aureus* (*MRSA*). In vivo assessments, the implant system was demonstrated with effective antibacterial property while inducing bone repair and osseointegration in infected bone defects. To our knowledge, this is the first time to construct a composite implant system with antibacterial and osteogenic dual-functions TEOS/AgNPs hydrogel and 3D printed Ti6Al4V scaffolds for the

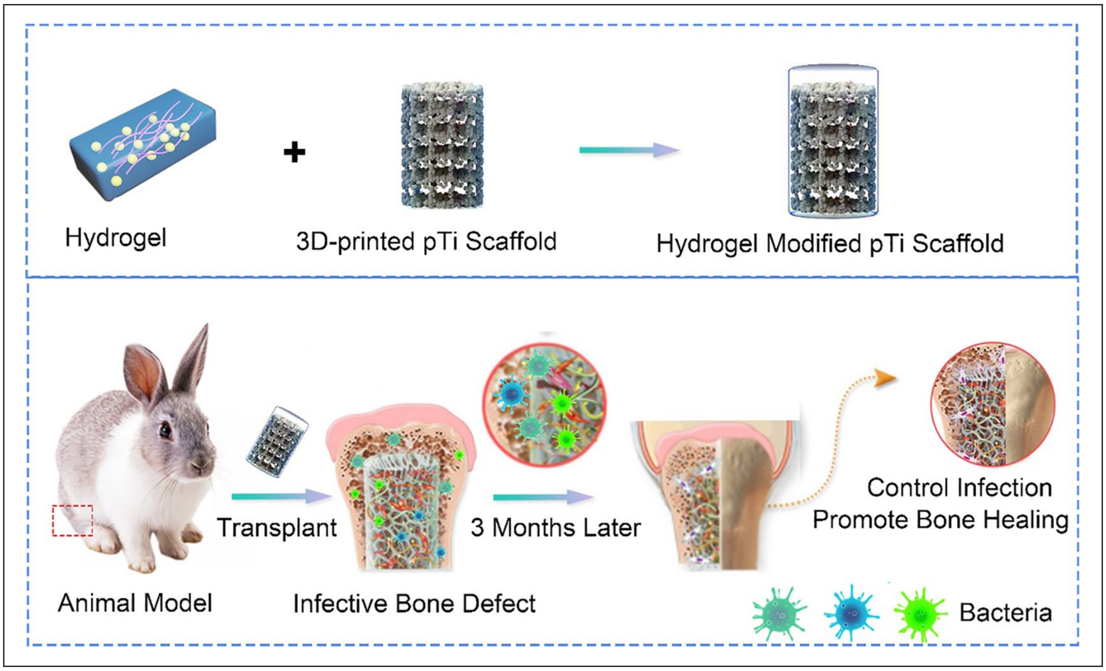

Scheme 1. The combination of supramolecular hydrogels with dual functions of antibacterial and induced osteogenesis and 3D printed pTi for infective bone defect treatment.

treatment of infected bone defects. The composite scaffold would open a novel avenue for exploring a new-generation of bone graft materials in infectious bone defects.

Materials and methods

Materials

Silver nitrate ($AgNO_3$, ≈99.8%), sodium tetraborate ($Na_2B_4O_7.10H_2O$), and sodium borohydride ($NaBH_4$, ≈96%) were obtained from Beijing Chemical Works (Beijing, China). Polyvinyl pyrrolidone (PVPON, Mw≈40 000), polyvinyl alcohol (PVA, ≈99% hydrolyzed, Mw ≈130000), and TEOS were purchased from Sigma-Aldrich. Hydrogen peroxide (H_2O_2, 30 wt%) was obtained from Beijing Chemical Works (Beijing, China). Ti_6Al_4V powder was supplied by AK Medical Co., Ltd. (Beijing, China). The *S. aureus* strain and *MRSA* strain, and rabbit BMSCs were supplied by American Type Culture Collection (ATCC, Maryland, USA). Dulbecco's Modified Eagle's Medium (DMEM, low glucose), streptomycin–penicillin, and fetal bovine serum (FBS) were supplied by Gibco® Life Technologies (CA, USA). Cell Counting Kit-8 (CCK-8) assay was purchased from Beyotime Biotechnology (Shanghai, China). Medium for osteogenic differentiation of rabbit BMSCs was obtained from Cyagen Biosciences (CA, USA). Phosphate buffer (PBS) and 4% paraformaldehyde were purchased from Solarbio (Beijing, China). Eastep Super Total RNA Extraction Kit was supplied by Promega (Shanghai, China), and Perfect Real Time RT reagent kit was provided by Takara Bio (Dalian, China). Live/Dead BacLight viability kit, Masson stain and Giemsa stain were got from Thermo Fisher Scientific (MA, USA).

Preparation of 3D printed pTi scaffolds

3D printed Ti_6Al_4V porous scaffolds were prepared by additive manufacturing technique *via* an EBM system (Q10, Arcam, Sweden) as previously reported.[34] Spherical titanium alloy powder (Grade 23, particle size 45–100 μm) was melted layer by layer according to the preset parameters. The pTi scaffolds were designed based on about 70% in porosity and about 600 μm in pore diameter. The scaffolds for microstructure observation and cell experiments in vitro were designed to be disk-shaped (ϕ10 mm × L3 mm), while columnar-shaped scaffolds (ϕ6 mm×L10 mm) were used for mechanical testing and osseointegration detections in vivo. All fabricated pTi scaffolds were ultrasonically cleaned and washed in acetone, ethyl alcohol, and deionized water for ~15 min for each treatment, and sequentially autoclaved for 30 min.

The porosity of samples was measured by Micro-CT (SkyScan 1076 scanner, Kontich, Belgium) and NRecon software (version 1.6.6; Bruker micro-CT). In order to analyze the diameter and distribution of the micropores, the microstructure of pTi scaffolds was captured by a scanning electron microscope (SEM, JEOL JSM-6700F, Japan), and the images were analyzed by Image Pro Plus 6.0 (NIH, MD, USA).

Preparation of multi-functional hydrogels

The hydrogel was synthesized by the following procedure. (1) Preparation of AgNPs: Preparation of AgNPs according to literature methods.[35,36] Briefly, PVPON aqueous solution (1 mL, 4.2 mM), sodium citrate aqueous solution (1 mL 180 mM) and 30% H_2O_2 (0.24 mL) were sequentially added into $AgNO_3$ aqueous solution (97 mL, 0.1 mM) with stirring. Subsequently, $NaBH_4$ aqueous solution (0.3 mL, 100 mL) was added to the above mixed solution with stirring. After stirring at room temperature for 30 mins, the AgNPs were synthesized. (2) Preparation of hydrogels: Different concentration of PVA was dissolved in deionized water under magnetic stirring at 90°C. Afterwards, an appropriate mass of AgNPs (0, 0.1, 0.2, and 0.3 mmol) and TEOS (0.4 mmol) were added to the above solution under vigorous stirring, respectively. After completely dissolved, $Na_2B_4O_7$ (10 mL, 0.04 mM) solution was injected into the mixture and further stirred for 10 mins at 90°C until the hybrid hydrogel was formed.

Rheological analysis

The rheology of the hydrogel was tested using a rheometer. The fixture uses a circular parallel plate with a diameter of 10 mm, and the gap is set to 1 mm. In the course of the experiment, in order to prevent the gel from drying out, the hydrogel can be covered with a lid to avoid water evaporation. When testing the hydrogel in time sweep mode, the frequency of the rheometer is set to 10 rad/s, the strain is set to 0.1%, and the temperature is set to 25°C. In the strain sweep mode, the frequency of the rheometer is set to 10 rad/s, the temperature is set to 25°C, and the strain is set in the range of 0.01% to 100%. Repeat measurement of at least three independent samples to ensure reproducibility.

Equilibrium swelling ratio

The equilibrium swelling ratio was detected by recording the change in wet weight during incubation in PBS at pH 7.4. In detail, the mass of the original wet hydrogel is recorded as W_0. Afterwards, the hydrogel was incubated in PBS at 37°C. At different time points, the hydrogels were extracted from the PBS, and the quality was recorded as Wt. The swelling rate calculation formula is: $(W_t–W_0)$ / $W_0 \times 100\%$. Repeat measurement of at least three independent samples to ensure reproducibility.

In vitro degradation experiments

The in vitro degradation rate was investigated by observing the change in dry mass of the hydrogel. Firstly, place the lyophilized hydrogel (50 mg) in a simulated physiological environment in vitro (phosphate buffer solution at 37°C). Add 0.02 wt% NaN_3 to the solution to inhibit the growth of bacteria. At different experimental time points, the residual hydrogels were collected and the mass loss was calculated after lyophilization. Repeat measurement of at least three independent samples to ensure reproducibility.

Biocompatibility

To evaluate on the biocompatibility of the composite scaffolds, CCK-8 assays were performed. The BMSCs were trypsinized and resuspended, then DMEM containing BMSCs (5×10^4 /well) suspension was added into a 24-well plate. BMSCs cultured without scaffolds were used as control group (abbreviated as Con) to study the biocompatibility of different scaffold complexes, and 3D printed pTi group was abbreviated as pTi. The hydrogel on pTi@L-Gel group formula is 10 wt% PVA, 0.20 mmol $Na_2B_4O_7$, 0.4 mmol TEOS and 0.1 mmol AgNPs (low concentration AgNPs). The hydrogel on pTi@M-Gel group formula is 10 wt% PVA, 0.20 mmol $Na_2B_4O_7$, 0.4 mmol TEOS and 0.2 mmol AgNPs (medium concentration AgNPs). The hydrogel on pTi@H-Gel group formula is 10 wt% PVA, 0.20 mmol $Na_2B_4O_7$, 0.4 mmol TEOS and 0.3 mmol AgNPs (high concentration AgNPs). For cell proliferation detection, CCK-8 assays were carried out after 1, 4, and 7 days of incubation at the atmosphere of 37°C and 5% CO_2. At the predetermined time interval, the DMEM medium was discarded, and 10% CCK-8 reaction solution was added into each well and incubated for 2 h at 37°C and 5% CO_2. Finally, 100 µl sample solution was taken out and placed into a 96-well plate for absorbance measure by the Multiskan EX Microplate Reader (Thermo Fisher Scientific, MA, USA) at 450 nm.

Modification multi-functional hydrogels on three-dimensional printed porous titanium alloys

10 wt% PVA was dissolved in deionized water (10 mL) under magnetic stirring at 90°C. Afterwards, an appropriate mass of AgNPs (0.1, 0.2, and 0.3 mmol) and TEOS (0.4 mmol) were added to the above solution under vigorous stirring, respectively. After completely dissolved, the above precursor solution (1 mL) was injected into a three-dimensional printed porous titanium alloy. Then, $Na_2B_4O_7$ (1 mL, 0.04 mM) solution was injected into the three-dimensional printed porous titanium alloy, and further vibrated for 10 minss at 90°C until the hybrid hydrogel was formed in pores of 3D printed pTi implants.

Osteogenic differentiation of BMSCs

To detect the osteogenic induction ability of this dual-function composite scaffolds, BMSCs were seeded in plate (Con), pTi, pTi@L-Gel, pTi@M-Gel, and pTi@H-Gel groups at a density of 5×10^5 cells for per well. After culture for 14 and 21 days by osteogenic induction medium, alizarin red (AR) staining was conducted to measure calcium deposition. And then, 10% cetylpyridinium chloride was incorporated into the dyed mineralized nodules to dissolve the stained calcium nodule for further semi-quantitative analysis. The obtained sample solution was measured at 450 nm by microplate reader.

In addition, the expression of osteogenic differentiation related genes, including alkaline phosphatases (*ALP*), runt-related transcription factor-2 (*Runx-2*), osteocalcin (*OCN*), and bone morphogenetic protein (*BMP-2*) were detected by real-time quantitative PCR (RT-qPCR) after osteogenic induction for 14 and 21 days. The sequences of primers were listed in Table S1. The amplification and detection of RT-qPCR was carried out by a LightCycler 480 through 2× Fast SYBR Green Master Mix (Roche Diagnostics, Basel, Switzerland). Relative mRNAs expression levels were normalized to that of GAPDH and calculated by the $2^{-}\Delta\Delta^{Ct}$ method.

Antibacterial assessment in vitro

S. aureus (ATCC25923) and *MRSA* (ATCC43300) suspension were used for bacterial proliferation and Live/Dead staining, at the density of 1.0×10^8 colony forming units (CFU)/mL. 1.0 mL bacterial suspension was inoculated uniformly into each tube. Next, different scaffolds (pTi, pTi@L-Gel, pTi@M-Gel, and pTi@H-Gel, respectively) was placed into the tubes and cultured with Luria Bertani (LB) medium at 37°C, and 100 r/min. The tubes without any scaffold and only bacterial solution were set as negative control group (Con). After 0, 12, 24, and 36 h of incubation, 100 µL samples were collected and the absorbance of bacterial solution was measured by a microplate reader (Multiskan EX, Thermo Fisher Scientific, Shanghai, China) at 600 nm. Furthermore, in order to estimate the antibiotic characterism, Live/Dead BacLight viability kit was carried out after 24 h of culture. The samples were incubated in the dilute dye solution for 15 mins at room temperature, and then fixed with 4% glutaraldehyde for 1 h, and photographed by confocal laser scanning microscope (CLSM, FV1000, Olympus, Japan).

Preparation of infected bone defect models

All animal procedures were examined and approved by the Animal Ethics Committee of Shanghai Ninth People's Hospital, Shanghai Jiaotong University. Thirty female New Zealand white rabbits (five months old) were used to establish infected bone defects models. An incision was made in the left femoral condyle under general anesthesia through ketamine (35 mg/kg) and xylazine (2 mg/kg) intramuscularly. After exposing the bony surface of the lateral condyle, cylindrical bone defects with 6 mm (diameter) ×10 mm (depth) were made by bone drills. Then, the 500 µl bacterial suspension containing 1.0×10^5 CFU *S. aureus* and 1.0×10^5 CFU *MRSA* was injected into the medullary cavity through the defects. After the defects implanted with pTi scaffolds or 3D printed pTi modified hydrogel with medium concentration AgNPs (abbreviated as pTi@M-Gel), the incisions were subsequently closed by absorbable sutures. No antibiotics were administered post-operatively.

On the day of operation and 6 weeks and 12 weeks after operation, venous blood was taken for White Blood Cell (WBC) count to evaluate systemic infection. At 6 weeks and 12 weeks post-implantation, rabbits were sacrificed, and femur samples were collected and preserved in 4% polyformaldehyde solution for further Micro-CT and histological examination.

Micro-CT analysis

To study the efficiency of bone regeneration, the samples were examined by Micro-CT scanning. Scanning parameters were as follows: 90 kV voltage, 114 mA current, and 18 µm pixel size. The cylindrical region of the pTi was selected as the region of interest (ROI, ϕ6 mm×L10 mm) for 3D reconstruction and parameter analysis. 3D reconstruction was carried out to observe the bone regeneration on the surface of different scaffolds. To estimate the quality of bone ingrowth, quantitative morphometric analysis of the columnar-shaped ROI was carried out by micro-CT auxiliary software (NRecon version 1.6.6), including parameters of bone volume/tissue volume ratio (BV/TV, %), trabecular thickness (Tb.Th, mm), trabecular number (Tb.N, 1/mm), and trabecular separation (Tb.Sp, mm).

Histological evaluation

The femur samples containing pTi scaffolds were embedded in methyl methacrylate, without undergoing decalcification, and sectioned into thin sections (150–300 µm thickness). The sections were ground down and polished to 40–50 µm, and the sections were stained with Masson's trichrome to observe the bone regeneration and integration. In addition, to evaluate the infection around the implants, the tissue on the surface of porous scaffold was scraped, and then Giemsa staining were performed to inspect the bacterial contamination.

Push-out test

The standard push-out test was performed to evaluate the bond strength of the bone-implant interface. The samples were placed on the plate for the detaching test at 0.1 mm/s using a Universal Testing Machine. The loading for the pTi scaffolds became detached from the bone was regarded as the maximum bond intensity between the host bone and pTi scaffolds.

Statistical analysis

All results were expressed as mean ± standard deviation (SD) from at least three independent experiments,

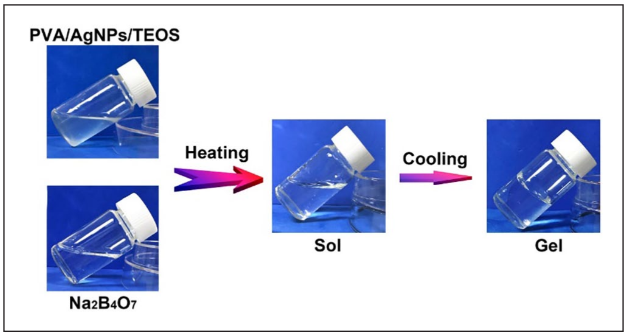

Figure 1. The photographs of the gelation progress. The mixture of prepared polyvinyl alcohol (PVA), silver nanoparticles (AgNPs) and tetraethyl orthosilicate (TEOS) solution presented in the sol state, and it experienced sol-gel transition after adding sodium tetraborate ($Na_2B_4O_7$) solution.

and analyzed by Student's *t*-test or one-way analysis of variance (ANOVA) with statistical software SPSS 19.0 (SPSS Inc., Chicago, USA). $P < 0.05$ was recognized to be statistically significant.

Results and discussion

The design strategy for the supramolecular hydrogels

To endow 3D printed pTi antibacterial ability and biological activity, we firstly synthesized a supramolecular hydrogel for modification of pTi. The synthetic process of the hydrogel was shown in Figure 1. Entirely dissolved polyvinyl alcohol, silver nanoparticles and tetraethyl orthosilicate were added to the solution of sodium tetraborate at 90°C. After cool to room temperature, the mixture solution was quickly experienced sol-gel transition. The hydrogels are generated from dynamic supramolecular assembly of sodium tetraborate, polyvinyl alcohol, silver nanoparticles and tetraethyl orthosilicate. The whole synthetic route is very simple, which do not involve the synthesis of complex molecules and the generation of toxic substances.

The mechanical performances of prepared hydrogels could be adjusted by changing the content of individual components. The gel dynamics of hydrogels with different concentrations were monitored by recording the storage modulus (G') and loss modulus (G") in time scan mode. The experimental results of the rheological analysis showed that as the PVA and $Na_2B_4O_7$ content increased, the G' and G" of hydrogels increased accordingly (Figure 2(a) and (b)). In contrast, the concentration of TEOS and AgNPs have a negligible impact on the dynamic properties of hydrogels. For further study the rheological properties of supramolecular hydrogels, the specific hydrogel was analyzed in strain scan mode (0.1%–1000%). As shown in Figure 2(c), in the low strain area, both G' and G" maintained at a constant value. As the strain increased, the G' and G" curves intersected at a strain of 17%, which is the required critical strain value to destruct the hydrogel network. When the strain further increased to 1000%, the G' and G" values dropped rapidly due to the collapse of the hydrogel network. Based on the strain amplitude scan results, we quantitatively analyzed the self-healing properties of the hydrogel (Figure 2(d)). Apply 100% and 1% continuously varying shear strains to the hydrogel, each with a duration of 150 s. It can be observed that at higher shear strains (100%), G" was always higher than G' implying the hydrogel was destroyed. Subsequently, when the shear strain dropped to 1%, G' and G" almost completely returned to the initial value within 150 s, indicating that the hydrogel network structure was restored. This process can be repeated multiple times, proving that supramolecular hydrogels have repeatable mechanical self-healing properties. In addition, we applied macroscopic observation to further demonstrate the self-healing property of the hydrogel. As displayed in Figure 2(e), the supramolecular hydrogels were dyed with Rhodamine B and methylene, and physically cut into two halves, respectively. Afterwards, the fresh halves were brought into contact. After 2 h of repair, the two separated hydrogels could form a complete hydrogel. This outstanding self-healing property is due to the dynamic nature of boronate formation between $Na_2B_4O_7$ and PVA.

We then investigated the swelling characteristics of the hydrogel under physiological conditions (i.e. phosphate buffer solution at 37° C). The hydrogel can reach swelling equilibrium in about 120 min, and the maximum swelling rate is about 15% (Figure 2(f)). Simultaneously, during the entire swelling process, the hydrogel can maintain its original shape with negligible mass loss. This physical and chemical stability is ideal for implantation. The degradability is also another important factor for implantation. By measuring the change of dry weight of hydrogel under physiological conditions, its in vitro degradation ability was evaluated. As shown in Figure 2(g), the supramolecular hydrogels completely degraded in 36 days demonstrating the biocompatibility of hydrogels.

Characterization of bioactive interface

The pTi scaffolds were successfully manufactured by 3D printing technology. Representative optical images of the pTi scaffolds were demonstrated in Figure 3(a) and (b), and then quantitative analysis performed by Image J indicated that the average pore size of the pTi was 598.4 ± 8.9 µm. According to the quantitative analysis of Micro-CT, the porosity of the pTi was 70.12 ± 0.64%. Therefore, the actual pore size and porosity was in line with the original design (600 µm and 70%, respectively). The porosity, pore size and distribution of the implants are closely related to the osteointegrative capacity. For bone tissue engineering, micropores with a diameter of 300 to 700 µm are favorable for cell adhesion, proliferation and osteogenic differentiation. While the porosity should be above 50%, especially

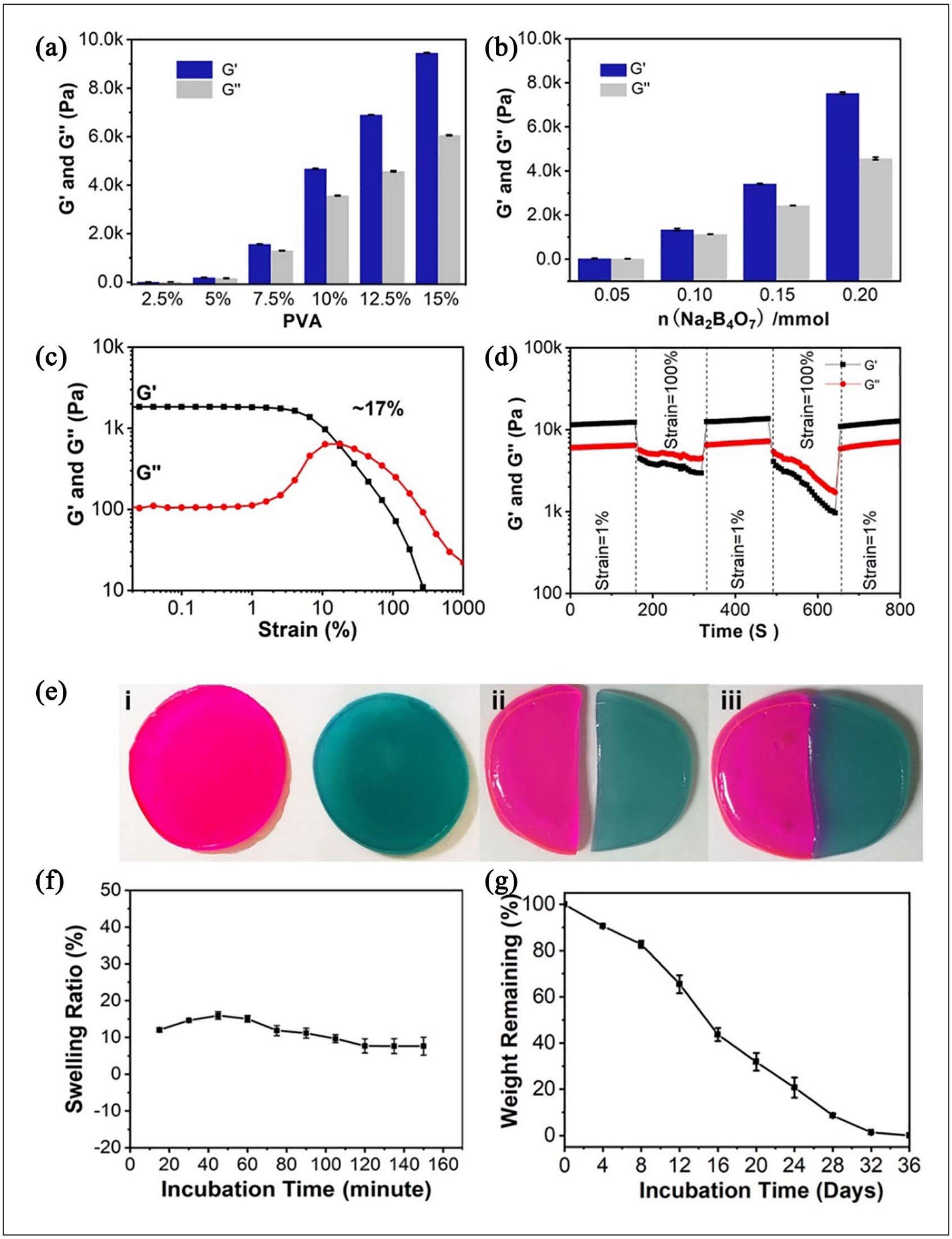

Figure 2. (a) The storage and loss modulus increase as the concentration of PVA increases from 2.5 to 12.5 wt % ($n = 3$). (b) The storage and loss modulus increase as the concentration of $Na_2B_4O_7$ increases from 0.05 to 0.20 mmol ($n = 3$). (c) The strain amplitude sweeps of the hydrogel. The hydrogel formula is 10 wt% PVA, 0.20 mmol $Na_2B_4O_7$, 0.4 mmol TEOS and 0.1 mmol AgNPs. (d) Step strain measurements of the hydrogel with a fixed frequency of 1 rad/s. (e) The macroscopic observation of self-healing property. (f) The equilibrium swelling ratio was tested by recording the change in wet weight during incubation under phosphate buffered saline (PBS, pH 7.4). (g) The in vitro degradation rate was measured by measuring the change in dry mass of the hydrogel. The hydrogel formula is 10 wt% PVA, 0.20 mmol $Na_2B_4O_7$, 0.4 mmol TEOS and 0.1 mmol AgNPs.

within 65% to 75%, which is structurally and mechanically similar to human trabecular bone.[37,38] Thus, the pore size and porosity of pTi in this study was a promising candidate for bone tissue engineering.

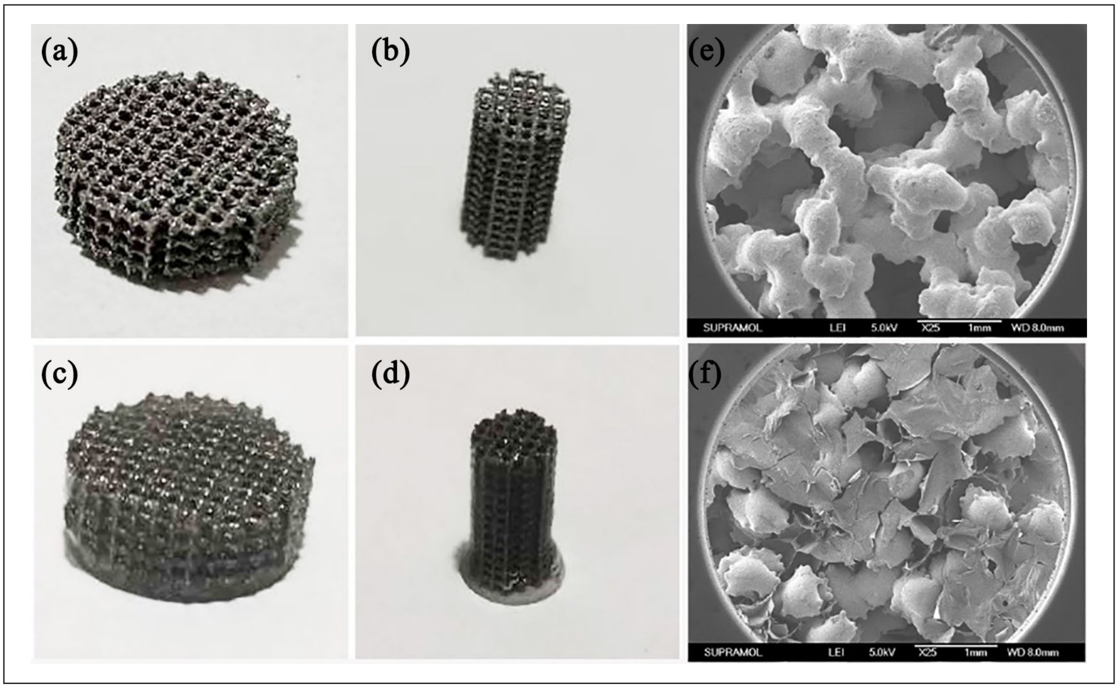

Figure 3. Visual images of (a) disk-shaped and (b) columnar-shaped pTi scaffolds. Visual images of supramolecular hydrogel modified (c) disk-shaped and (d) columnar-shaped pTi scaffolds. SEM microphotographs of (e) pTi scaffolds and (f) supramolecular hydrogel modified pTi scaffolds.

However, the porous structure also provides an absolute place for bacterial reproduction,[10] and pTi scaffold lacks of bioactivities for native stem cells survival, differentiation, and communication. To solve problems of infection and bioinertness, we modified the above 3D printed metal scaffold with the prepared supramolecular hydrogel. The specific method was to inject the precursor solution of PVA, AgNPs and TEOS into the pTi, and then added $Na_2B_4O_7$ solution to polymerize. As a result, the 3D composite implant system was obtained (Figure 3(c) and (d)). The high-resolution XPS spectrum of Ag 3d at 367.6 and 373.5 eV are assigned to Ag (0) and Ag (I) (Figure S1), respectively, demonstrating that Ag NPs were on the surface of scaffolds. The morphology and microarchitecture of scaffolds have profound effects on their functions during the biomedical applications. For comparison, SEM was applied to investigate the microstructure of pTi and supramolecular hydrogel modified pTi. As shown in Figure 3(e) and (f), increased surface area and porosity of the scaffolds could enhance the initial stability of the implant, improve the friction coefficient between the bone and scaffolds to reduce micromotion, induce bone ingrowth and promote osseointegration after implanting in vivo.[39] In addition, the lyophilized supramolecular hydrogels have a homogeneous and porous network structure (Supplemental Figure S2). These nanochannels of hydrogels on the pTi scaffolds could benefit oxygen and nutrient transportation, thereby improving cells survival and communication, which has important value for biological applications.[40]

BMSCs number on 3D printed composite pTi scaffolds

The BMSCs number on 3D printed composite pTi scaffolds was detected by the CCK-8 assays. For comparison, we set up a blank control group (abbreviated as Con), 3D printed pTi (abbreviated as pTi), 3D printed pTi modified hydrogel with low concentration AgNPs (abbreviated as pTi@L-Gel), 3D printed pTi modified hydrogel with medium concentration AgNPs (abbreviated as pTi@M-Gel), and 3D printed pTi modified hydrogel with high concentration AgNPs (abbreviated as pTi@H-Gel). The results demonstrated that cell numbers in the Con, pTi, pTi@L-Gel, and pTi@M-Gel groups increased gradually without significant difference between each other at 1, 4, and 7 days in vitro culture (Figure 4). Thus, a relative long-term release of AgNPs with suitable concentration may not inhibit the cell proliferation, which provides evidence that the pTi@L-Gel and pTi@M-Gel composite systems have no obvious cytotoxicity for BMSCs.[41] While the pTi@H-Gel group exhibited an inhibitory effect on the cell viability on day 7, compared to Con, pTi, pTi@L-Gel, and pTi@M-Gel groups ($p < 0.05$), which caused by the high concentration of AgNPs in the combination system.

Osteogenic differentiation assessment

Except for good biocompatibility, the effect on cells' osteoblastic differentiation is a crucial issue for a qualified bone tissue engineering implant. Osteogenic differentiation is characterized by calcium deposits, which was indicated by AR staining.[34] As demonstrated in Figure 5(a), BMSCs cultured with hydrogel incorporated pTi scaffolds (pTi@L-Gel and pTi@M-Gel groups) were strongly stained by AR, especially after 21 days of incubation. However, this mineralization rate slowed down in pTi@H-Gel group at 21 days, compared with pTi@L-Gel and pTi@M-Gel groups. In the Con and pTi groups showed limited staining on day 14, although the calcium nodules increased on the 21st day, it was still less than that of the composite scaffold groups. The following semi-quantitative analysis of AR staining further confirmed this difference. More calcium deposition was detected in the pTi@L-Gel, pTi@M-Gel, and pTi@H-Gel groups than that in the Con group at 14 days ($p < 0.05$). On the day 21, the absorbance value of pTi@L-Gel and pTi@M-Gel was not only significantly higher than pTi and Con groups, but also higher than pTi@H-Gel group (Supplemental Figure S3). Interestingly, the mineralization degree of pTi group was similar to that of pTi@H-Gel group at two time points, and was better than Con group on the 21st day. These findings revealed that the pTi@L-Gel and pTi@M-Gel groups promoted the formation of mineralized matrix.

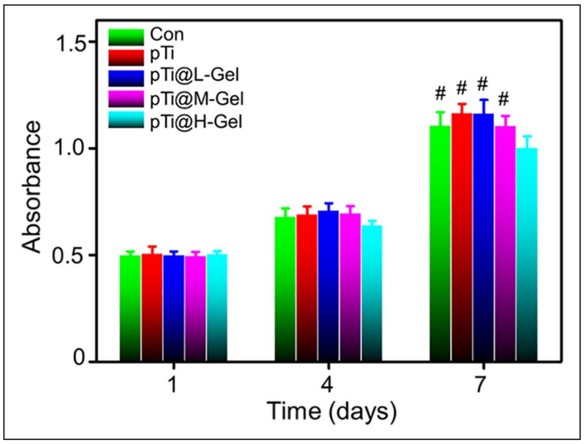

Figure 4. CCK-8 analysis of BMSCs number on Con, pTi, pTi@L-Gel, pTi@M-Gel, and pTi@H-Gel groups ($^{\#}p < 0.05$ compared with the pTi@H-Gel group). The hydrogel on pTi@L-Gel group formula is 10 wt% PVA, 0.20 mmol $Na_2B_4O_7$, 0.4 mmol TEOS and 0.1 mmol AgNPs. The hydrogel on pTi@M-Gel group formula is 10 wt% PVA, 0.20 mmol $Na_2B_4O_7$, 0.4 mmol TEOS and 0.2 mmol AgNPs. The hydrogel on pTi@H-Gel group formula is 10 wt% PVA, 0.20 mmol $Na_2B_4O_7$, 0.4 mmol TEOS and 0.3 mmol AgNPs.

In addition, a series of critical osteogenic markers for BMSCs cultured with scaffolds were examined by qPCR assay. *ALP* is evaluated to reveal the osteogenic differentiation, and the activation of *ALP* activity is a crucial event happening in early osteogenesis.[42] The results showed the increased transcriptional expression of *ALP* in either pTi@L-Gel, pTi@M-Gel, and pTi@H-Gel groups at 14 days compared with Con group. Moreover, at 21st day, *ALP* was found enhanced in pTi@L-Gel and pTi@M-Gel groups compared with both Con and pTi groups. While, the *ALP* expression in pTi@H-Gel group showed no

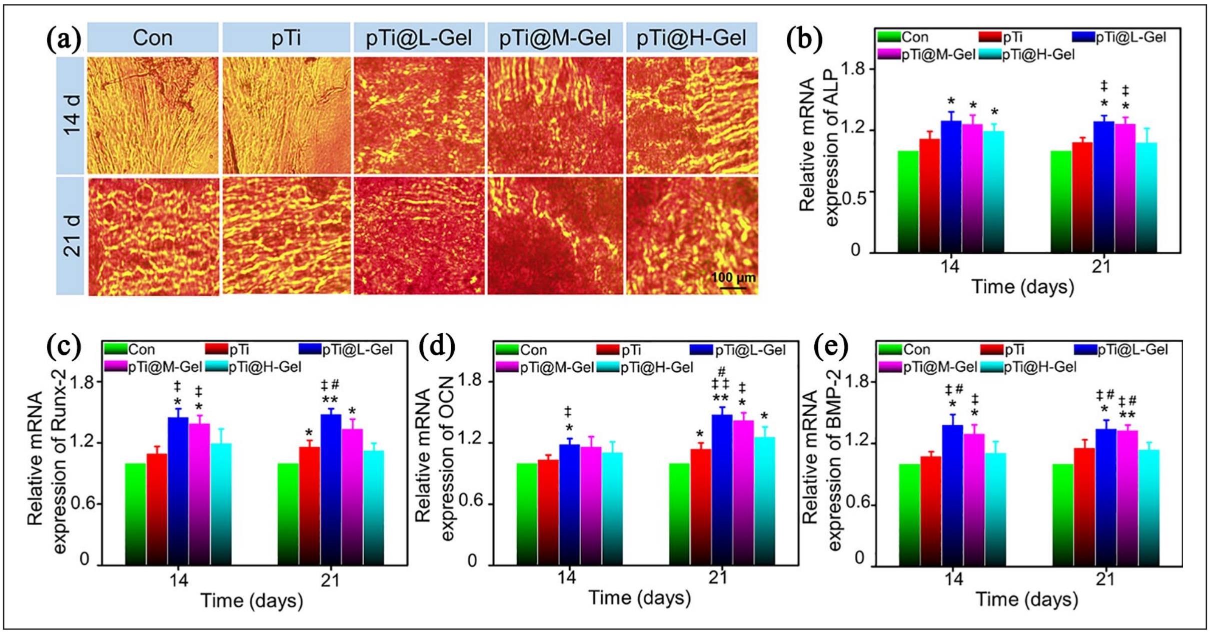

Figure 5. Osteogenic differentiation evaluation of various scaffolds. (A) AR staining of BMSCs cultured in the different scaffolds after osteogenic induction for 14 and 21 days. Relative mRNA expression of osteogenic differentiation-related genes in BMSCs cultured in various of scaffolds measured by real-time PCR after 14 and 21 days induction: (B) ALP, (C) Runx-2, (D) OCN and (E) BMP-2. ($^{*}p < 0.05$, $^{**}p < 0.01$ compared with the Con group. $^{\ddagger}p < 0.05$, $^{\ddagger\ddagger}p < 0.01$ compared with the pTi group. $^{\#}p < 0.05$ compared with the pTi@H-Gel group).

significant change compared with Con and pTi groups at 21 days (Figure 5(b)). *Runx-2* is another marker of the earliest osteoblastic differentiation, which can induce other osteogenic related genes up-regulation like *OCN* and osteopontin (*OPN*).[43] As demonstrated in Figure 5(c), *Runx-2* was enhanced at the mRNA level in pTi@L-Gel and pTi@M-Gel groups after 14 and 21 days. Meanwhile, *Runx-2 in* pTi@H-Gel group did not exhibit a higher level than that in any other group. *OCN* is a type of bone-specific protein synthesized by osteoblasts and regarded as a relatively late osteogenic marker to estimate the osteogenic maturation and bone formation, and it expresses with the most abundant level at the late process of osteogenesis.[42] The expression of *OCN* was increased gradually with the prolongation of incubation time, and peaked at day 21 in the pTi@L-Gel and pTi@M-Gel groups. At days 14, BMSCs grown on the pTi@L-Gel scaffolds exhibited an obviously upregulated expression level of *OCN* compared to Con and pTi groups ($p < 0.05$). Moreover, at day 21, the expression of *OCN* in all pTi groups was also increased compared to that in the Con group ($p < 0.05$). In addition, pTi@l-Gel group induced a relatively enhanced level of *OCN* compared to pTi@H-Gel group in 21 days (Figure 5(d)). At the same time, the expression levels of *BMP-2*, which is one of the most fundamental osteoinductive factors and recognized to activate the BMSCs differentiation into osteoblasts,[44] was evidently increased in pTi@L-Gel and pTi@M-Gel groups compared to those in Con and pTi groups in either 14 or 21 days. Compared with pTi@H-Gel group, the expression level of *BMP-2* was found increased at 1.26-fold in pTi@L-Gel on day 14, further increased at 1.18-fold in pTi@L-Gel and at 1.17-fold in pTi@M-Gel group at day 21 (Figure 5(e)).

Based on the positive effects of silicon on bone, different silica-based materials, such as silicon dioxide thin film, nanosilicates, nanofibers, have been regarded as a potential bone substitutes.[45] Recently, a sequence of studies have focused on the bioactive silicon (Si) ions to induce cell proliferation and osteogenic differentiation.[46] The Si ions released from biomaterials could effectively enhance the secretion of angiogenic factors and induce mesenchymal stem cells osteogenic differentiation.[47] BMSCs were co-cultured with Si containing 3D printed composite system to explore the ability of osteogenic differentiation. The results confirmed that the composite system could significantly promote mineralization and up-regulate the expression levels of osteogenesis related genes, even in the presence of an appropriate concentration of AgNPs.

Antibacterial assessment

S. aureus and *MRSA* are the common causative microorganism in bone and joint infection.[48] Herein, we detected the in vitro antibacterial efficacy of TEOS/AgNPs @pTi scaffolds by absorbance evaluation bacterial proliferation and Live/Dead staining. The proliferation profile of *S. aureus* (Figure 6(a)) showed that TEOS/AgNPs @pTi scaffolds had a strong inhibitory effect on bacterial proliferation within 36 h compared with Con and pTi group, owing to the strong antibacterial effect of AgNPs on *S. aureus*. The initial release of AgNPs from antibacterial hydrogel is enough to inactivate all *S. aureus* in the system and can not continue to proliferate. However, the inhibitory effect of antibacterial hydrogel on *MRSA* was a little bit different. At the initial stage of 12 h, the inhibitory effect of antibacterial hydrogel on *MRSA* proliferation was not as obvious as that of *S. aureus*. With the increase of AgNPs release, the absorbance of bacteria decreased at 24 to 36 h, indicating that the antibacterial effect began obviously (Figure 6(b)), reflecting the slow release effect of the effluent gel system on AgNPs. It should be noted that bacteria proliferated increasingly in the pTi group than in the control group at 36 h ($p < 0.05$), which may due to the porous structure providing a place for bacterial reproduction.[10]

CLSM showed that lived bacteria with undamaged membranes were stained with green and dead bacteria with impaired membranes that appeared in red, respectively.[49] After culturing for 24 h, the immunofluorescence images indicated that most of the *S. aureus* (Figure 6(c)) and *MRSA* (Figure 6(d)) cultured in the Con and pTi groups were alive, suggested that 3D printed pTi had no antibacterial property. While bacteria cultured in the TEOS/AgNPs @pTi scaffolds were almost dead. In pTi@L-Gel, pTi@M-Gel, and pTi@H-Gel groups, with the increase of Ag irons concentration in hydrogels, they showed a better bacteriostatic effect.

Anti-infective effects in infectious bone defects

Dealing with bone defects with infection remains a great clinical challenge.[50] Although many treatments have been attempted, such as surgical debridement, antibiotic spacer, as well as vascularized bone graft, the antibacterials loaded poly(methyl methacrylate) (PMMA) bone cement is considered as the gold standard for both therapy and prophylaxis of infective bone defects.[51,52] But limited by the absence of biodegradability and osteoconductivity, the antibacterials loaded PMMA always failed to display priority in preventing and treating infected bone defects.[53] Implants with both osteoconductivity and broad spectrum antibiotic activity may act as a reasonable substitution in this condition.[54] While the effective antibiotic-loaded bone substitutes are still not available due to the multi-antibiotic-resistant organisms, unreliable osteoconductivity, and incompatible biomechanical properties.[55] To solve these challenges, a dual osteogenic and antibacterial conducive scaffold was developed by loading TEOS (bone induction factor) and AgNPs (antibacterial agent), to porous Ti_6Al_4V scaffold prepared by 3D printed method in the present study.

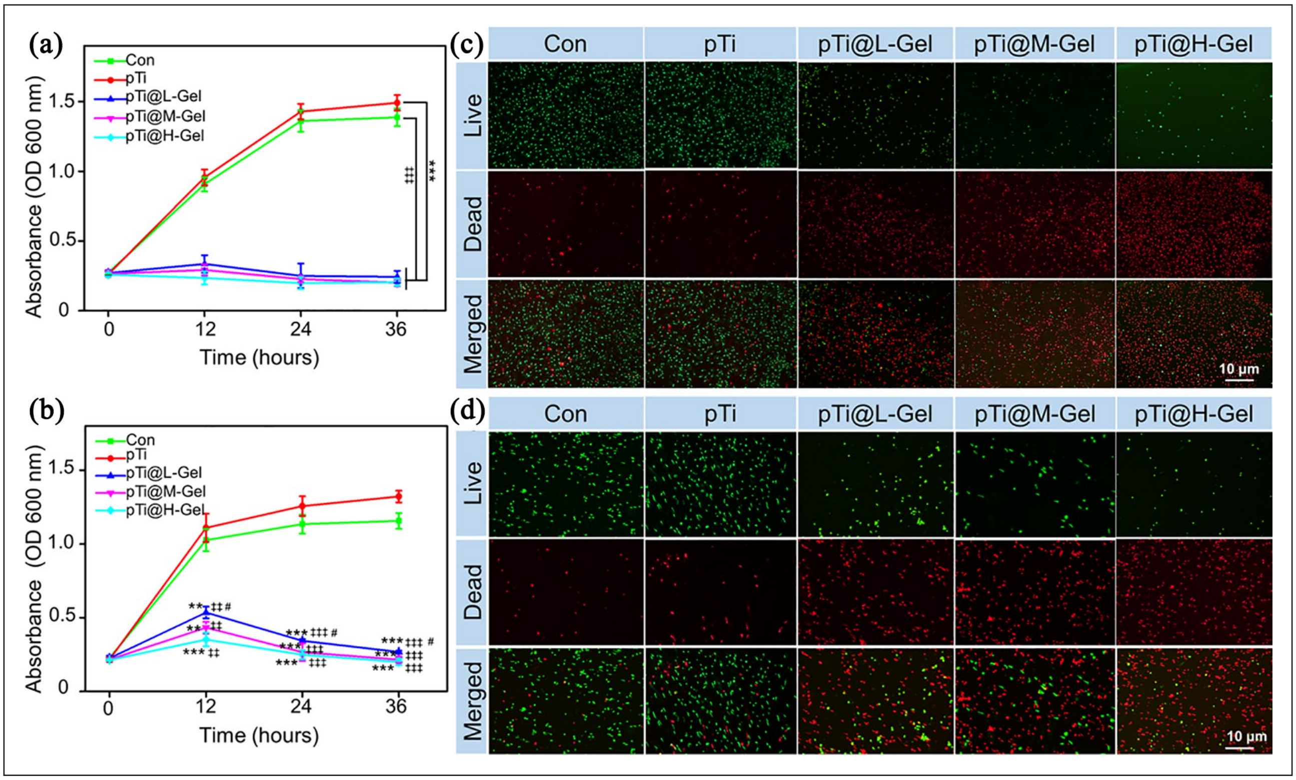

Figure 6. Antibacterial evaluation in vitro. Bacterial proliferation of (a) *S. aureus* and (b) *MRSA* co-cultured with different scaffolds. BacLight dead/live staining of (c) *S. aureus* and (d) *MRSA* co-cultured with different scaffolds for 24 h. Dead bacteria with impaired membranes appeared fluorescent red, and live bacteria with intact membranes appeared fluorescent green. ($^{**}p < 0.01$, $^{***}p < 0.001$ compared with the Con group. $^{‡‡}p < 0.01$, $^{‡‡‡}p < 0.001$ compared with the pTi group. $^{\#}p < 0.05$ compared with the pTi@H-Gel group).

As shown in Supplemental Figure S4, there was pus exudation on the surface of the operative wounds in pTi group, while the wounds of the pTi@M-Gel group healed well, and the wounds were covered by the regenerated hair at 12 weeks. We tested the WBC count in the peripheral blood to evaluate the systemic inflammation after bacterial and scaffolds implantation. Hematological examination on the day before the implantation showed that the WBC number in the two groups was in the physiological range. However, as shown in Figure 7(a), at 6 and 12 weeks post-implantation, the leukocytes in pTi group increased continuously with the prolongation of implantation time, which was significantly increased compared with that in pTi@M-Gel group ($p < 0.05$). These results demonstrated that the local release of AgNPs can restrict the growth of bacteria in the marrow cavity and control the systemic spread of infection. The infection around the metal implants seriously affect the osseointegration between the host bone and the prosthesis. Therefore, we detected the bacterial residue in the tissue around the scaffolds by Giemsa staining. Amount of bacteria were found in the Giemsa stained slices in pTi group at 6- and 12-weeks post-operation. Excitingly, in pTi@M-Gel group, it was difficult to find bacteria residues in the tissues around scaffolds (Figure 7(b)).

S. Aureus is the most common microorganism from bone infection.[56] The detection rate of *S.aureus* in pyogenic osteomyelitis reaches 80% to 90%.[57] It is also worth noting that the proportion of bone infection caused by *MRSA* increased.[58,59] AgNPs is a broad-spectrum antimicrobial, which against microorganisms through multiple mechanisms, thus greatly decreasing the chance of drug resistance. Compared with ionic silver, AgNPs has a more superior antimicrobial performance owing to their better permeation and retention effects.[33] The toxicity of AgNPs could kill bacteria, but also has an influence on normal cells, which shows a concentration dependent cytotoxic effect.[60] For this reason, to design a therapeutic window to control AgNPs within a range, which can inhibit bacteria but not produce toxicity to normal cells, is the critical issue for the application of AgNPs contained hydrogel. Considering the adverse effects of high concentration of AgNPs on cell proliferation and osteogenic differentiation, and low concentration of AgNPs not sufficient to inhibit bacteria, we selected the hydrogel with medium concentration AgNPs to composite the pTi (pTi@M-Gel) in vivo studies. Antibacterial experiments in vivo indicated that pTi scaffolds composite hydrogel containing a moderate concentration of AgNPs could significantly inhibit the

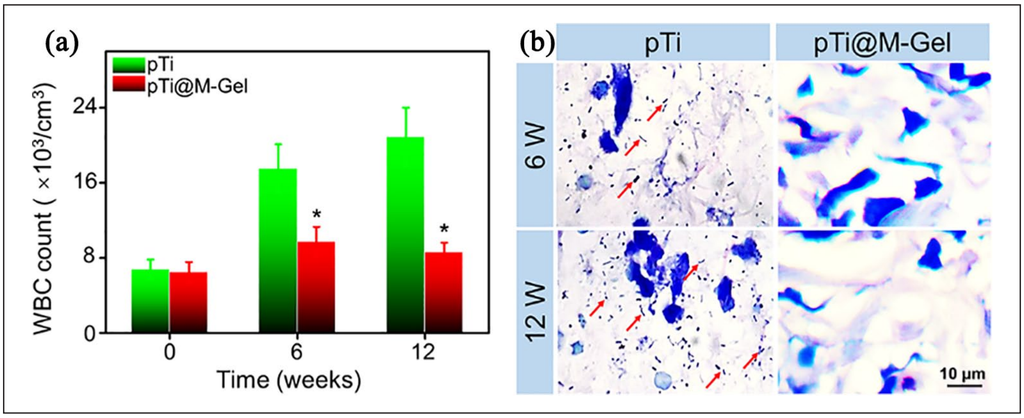

Figure 7. (a) WBC count in the peripheral blood to evaluate the systemic infection state. (b) Giemsa staining was carried out to assess bacterial contamination in the tissue around the surface of the scaffolds (red arrows indicate bacteria) (*$p < 0.05$ compared with the pTi group).

bacteria proliferation locally and prohibit the spread of infection systematically.

Bone regeneration in infectious bone defects

As for biomaterials applied for infectious bone defects, in addition to controlling local infection, the characterization to promote bone regeneration is another critical issue.[61] Herein, Micro-CT, Masson staining of hard tissue sections, and the push-out test was conducted to estimate the effects of composite scaffolds on bone regeneration and osseointegration of infectious bone defects at 6 and 12 weeks after implantation. The 3D reconstruction of the Micro-CT images of the distal femur samples collected from the bare pTi group after 6 weeks exhibited that the bone formation on the surface of the scaffold was limited, and the bone mass was without increasing significantly after 12 weeks post-implantation. However, in pTi@M-Gel group, more regenerated bone tissue was reconstructed on the surface of scaffolds and in micropores for 6 and 12 weeks, compared to the pTi group (Figure 8(a)). To quantify the bone ingrowth, the ROI (the implanted region and empty defect area) was analyzed by Micro-CT auxiliary software. The BV/TV values of pTi and pTi@M-Gel groups were 4.92 ± 0.82% and 11.19 ± 1.58% at 6 weeks, and 5.84 ± 1.07% and 18.24 ± 1.93% at 12 weeks (Figure 8(b)), separately, which were consistent with the results of 3D reconstruction images. In parallel, pTi@M-Gel group was found significant higher values of Tb.Th and Tb.N (Figure 8(c) and (d)) and an evident lower values of Tb.Sp compared to the pTi group (Figure 8(e)) at 6 and 12 weeks. Micro-CT results indicated that bone defects in the infectious microenvironment were difficult to regenerate effectively, and dual functional hydrogel composited pTi scaffolds could significantly reverse the poor bone formation compared with bare pTi scaffold.

Subsequently, the hard tissue sections were stained with Masson to measure the bone ingrowth into the microporous scaffolds. Better bone formation was found between the regenerated bone and the surface of pTi scaffolds without gaps in the pTi@M-Gel group, wherein bone tissue almost completely surrounded the surface of the implantations along with partial ingrowth into the inner pores, especially 12 weeks after implantation. However, a great quantity of yellow pus was found in the pores of bare pTi without antibacterial property, and the regenerated bone tissue was very limited around the scaffolds (Figure 8(f)). Good osseointegration between implants and host bone tissues involves a series of complicated biological processes. The ideal implantation should integrate with the surrounding bone tissue with strong mechanical combination to avoid complications of loosening and displacement after arthroplasty, and restore the functionality of reconstructed joints. To compare the bonding strength between the host bone and pTi, the push-out test was carried out (Figure 8(f)). At 6 weeks, the maximum loading of pTi@M-Gel group had significantly increased by 2.61-fold ($p < 0.01$) at 6 weeks and 2.89-fold ($p < 0.01$) compared with pTi groups, respectively.

Although the 3D printed titanium alloy microporous structure is beneficial for bone regeneration, it does not provide good osseointegration in an infectious microenvironment where is not conducive to bone regeneration. Therefore, elements with osteogenic properties are regarded as supplementary ingredients incorporating into scaffolds to achieve a better osteointegration.[62] Silicon, an essential trace element in the human body, has been indicated to play a critical role in bone formation and osteointegration. Within the cells, Si is distributed in the mitochondria and other intracellular organelles, and plays as a cross-linker between collagen and proteoglycans to induce the secretion of type I bone collagen (Col-1) and promote bone mineralization at the early stage of bone formation.[63] Furthermore, Si ions can stimulate osteogenesis and angiogenesis by regulating cell-cell interactions, stem cell migration, and differentiation.[64] Considering that the pivotal role of Si element in

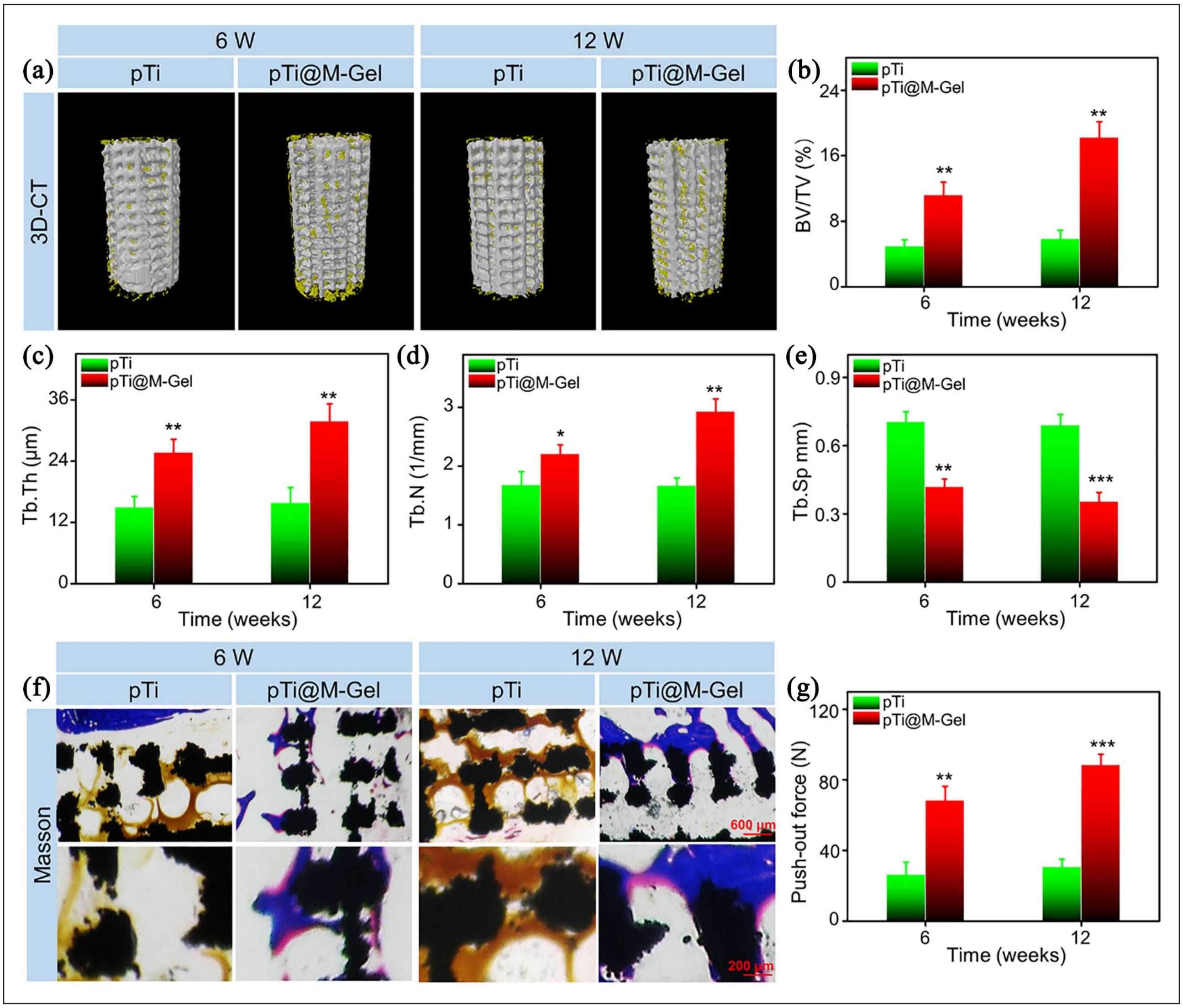

Figure 8. (a) 3D reconstruction images of porous implants (white) and regenerated bone tissue (yellow). Quantitative analysis of (b) BV/TV, (C) Tb.Th, (D) Tb.N, and (e) Tb.Sp of pTi and pTi@M-Gel groups according to Micro-CT at 6 and 12 weeks post-implantation. (f) Representative histological images Masson staining (The black areas indicated the pTi scaffolds, the blue areas indicated the bone, and the yellow areas was pus). (g) Evaluation of osseointegration through pull-out biomechanical testing after implantation for 6 and12 weeks (*$p < 0.05$, **$p < 0.01$, ***$p < 0.001$ compared with the pTi group).

osteogenesis, the employment of the Si in the design of the implants is highly pursued. Herein, we incorporated Si containing hydrogel into 3D printed metal microporous scaffolds and the results revealed that this composite scaffold conducive to bone regeneration significantly induced bone integration between the bone and pTi surface and improved the long-term stability. Moreover, the in vitro and in vivo investigations including inhibiting bacteria and inducing BMSCs differentiation and mineralization indicated that the hydrogel composited pTi was the ideal candidate for promoting new bone formation in the infection defects. Therefore, it is predicted that the 3D printed microporous system with antibacterial properties may have a potential in the treatment of bone defects with infectious or high risk of infection.

Conclusion

We fabricated an innovative, multifunctional supramolecular hydrogel, prepared from the dynamic supramolecular assembly of $Na_2B_4O_7$, PVA, AgNPs, and TEOS, and composited with 3D printed Ti_6Al_4V scaffolds as an implant system with the antibacterial ability and biological activity. The implant system demonstrated effective antibacterial ability while promoting bone regeneration and osseointegration in infected bone defects. This 3D composite implant system has the potential to control infection and promote bone healing in contaminated defects.

Author contributions

ShiC Qiao and **Dongl Wu:** Conceptualization; Data curation; Project administration; Resources; Software; Writing - original draft; **Zuh Li**: Data curation; Formal analysis; Investigation; Project administration; **Yu Zhu:** Formal analysis; Validation; **Hongc Lai:** Funding acquisition; Supervision; **Yingx Gu:** Conceptualization; Funding acquisition; Supervision; Writing - review & editing.

Declaration of conflicting interests

The author(s) declared no potential conflicts of interest with respect to the research, authorship, and/or publication of this article.

Funding

The author(s) disclosed receipt of the following financial support for the research, authorship, and/or publication of this article: This study has been supported by Science and Technology Commission of Shanghai Municipality (16441903600, 20S31906100), National Natural Science Foundation of China (81600902), Clinical Research Plan of SHDC 16CR3033A and Multicenter Clinical Research Program of Shanghai Jiao Tong University School of Medicine (DLY201822). Thanks for the support of Shanghai Zammax Biotech Co., Ltd.

ORCID iD

Zuhao Li https://orcid.org/0000-0003-1909-2999

Supplemental material

Supplemental material for this article is available online.

References

1. Zou F, Jiang J, Lv F, et al. Preparation of antibacterial and osteoconductive 3D-printed PLGA/Cu(I)@ZIF-8 nanocomposite scaffolds for infected bone repair. *J Nanobiotechnol* 2020; 18(1): 39.
2. Nair MB, Kretlow JD, Mikos AG, et al. Infection and tissue engineering in segmental bone defects−a mini review. *Curr Opin Biotechnol* 2011; 22(5): 721–725.
3. Okike K and Bhattacharyya T. Trends in the management of open fractures. A critical analysis. *J Bone Joint Surg Am Vol* 2006; 88(12): 2739–2748.
4. Mouriño V and Boccaccini AR. Bone tissue engineering therapeutics: controlled drug delivery in three-dimensional scaffolds. *J Roy Soc Interface* 2010; 7(43): 209–227.
5. Inzana JA, Schwarz EM, Kates SL, et al. Biomaterials approaches to treating implant-associated osteomyelitis. *Biomaterials* 2016; 81: 58–71.
6. Bai H, Zhao Y, Wang C, et al. Enhanced osseointegration of three-dimensional supramolecular bioactive interface through osteoporotic microenvironment regulation. *Theranostics* 2020; 10(11): 4779–4794.
7. Li L, Li Y, Yang L, et al. Polydopamine coating promotes early osteogenesis in 3D printing porous Ti6Al4V scaffolds. *Ann Transl Med* 2019; 7(11): 240.
8. Nune KC, Kumar A, Murr LE, et al. Interplay between self-assembled structure of bone morphogenetic protein-2 (BMP-2) and osteoblast functions in three-dimensional titanium alloy scaffolds: stimulation of osteogenic activity. *J Biomed Mater Res A* 2016; 104(2): 517–532.
9. Pan S, Yin J, Yu L, et al. 2D MXene-integrated 3D-printing scaffolds for augmented osteosarcoma phototherapy and accelerated tissue reconstruction. *Adv Sci (Weinh)* 2020; 7(2): 1901511.
10. Pariza G, Mavrodin CI and Antoniac I. Dependency between the porosity and polymeric structure of biomaterials used in hernia surgery and chronic mesh - infection. *Mater Plast* 2015; 52(4): 484–486.
11. Zhao Y, Wang Z, Jiang Y, et al. Biomimetic composite scaffolds to manipulate stem cells for aiding rheumatoid arthritis management. *Adv Funct Mater* 2019; 29(30): 1807860.
12. Pan G, Sun S, Zhang W, et al. Biomimetic design of mussel-derived bioactive peptides for dual-functionalization of titanium-based biomaterials. *J Am Chem Soc* 2016; 138(45): 15078–15086.
13. Yu Y, Yuk H, Parada GA, et al. Multifunctional “hydrogel skins” on diverse polymers with arbitrary shapes. *Adv Mater* 2019; 31(7): e1807101.
14. Zhu Y, Zhang J, Song J, et al. A multifunctional pro-healing zwitterionic hydrogel for simultaneous optical monitoring of pH and glucose in diabetic wound treatment. *Adv Funct Mater* 2019; 30(6): 1905493.
15. Wang L, Zhang X, Yang K, et al. A novel double-crosslinking-double-network design for injectable hydrogels with enhanced tissue adhesion and antibacterial capability for wound treatment. *Adv Funct Mater* 2019; 30(1): 1904156.
16. Zhao X, Chen F, Li Y, et al. Bioinspired ultra-stretchable and anti-freezing conductive hydrogel fibers with ordered and reversible polymer chain alignment. *Nat Commun* 2018; 9(1): 3579.
17. Yang C and Suo Z. Hydrogel ionotronics. *Nat Rev Mater* 2018; 3(6): 125–142.
18. Chen G, Yu Y, Wu X, et al. Bioinspired multifunctional hybrid hydrogel promotes wound healing. *Adv Funct Mater* 2018; 28(33): 1801386.
19. Zhao Z, Fang R, Rong Q, et al. Bioinspired nanocomposite hydrogels with highly ordered structures. *Adv Mater* 2017; 29(45): 1703045.
20. Zhang X, Wang J, Jin H, et al. Bioinspired supramolecular lubricating hydrogel induced by shear force. *J Am Chem Soc* 2018; 140(9): 3186–3189.
21. Bhattacharya S and Samanta SK. Soft-nanocomposites of nanoparticles and nanocarbons with supramolecular and polymer gels and their applications. *Chem Rev* 2016; 116(19): 11967–12028.
22. Zhao Y, Shi C, Yang X, et al. pH- and temperature-sensitive hydrogel nanoparticles with dual photoluminescence for bioprobes. *ACS Nano* 2016; 10(6): 5856–5863.
23. Liang Y, Zhao X, Hu T, et al. Adhesive hemostatic conducting injectable composite hydrogels with sustained drug

release and photothermal antibacterial activity to promote full-thickness skin regeneration during wound healing. *Small* 2019; 15(12): e1900046.

24. Ghobril C and Grinstaff MW. The chemistry and engineering of polymeric hydrogel adhesives for wound closure: a tutorial. *Chem Soc Rev* 2015; 44(7): 1820–1835.
25. Gan D, Huang Z, Wang X, et al. Graphene oxide-templated conductive and redox-active nanosheets incorporated hydrogels for adhesive bioelectronics. *Adv Funct Mater* 2019; 30(5): 1907678.
26. Baytekin HT, Baytekin B, Huda S, et al. Mechanochemical activation and patterning of an adhesive surface toward nanoparticle deposition. *J Am Chem Soc* 2015; 137(5): 1726–1729.
27. Flegeau K, Pace R, Gautier H, et al. Toward the development of biomimetic injectable and macroporous biohydrogels for regenerative medicine. *Adv Colloid Interface Sci* 2017; 247: 589–609.
28. Liu K, Han L, Tang P, et al. An anisotropic hydrogel based on mussel-inspired conductive ferrofluid composed of electromagnetic nanohybrids. *Nano Lett* 2019; 19(12): 8343–8356.
29. Wang C, Hu K, Zhao C, et al. Customization of conductive elastomer based on PVA/PEI for stretchable sensors. *Small* 2020; 16(7): e1904758.
30. Rittikulsittichai S, Kolhatkar AG, Sarangi S, et al. Multi-responsive hybrid particles: thermo-, pH-, photo-, and magneto-responsive magnetic hydrogel cores with gold nanorod optical triggers. *Nanoscale* 2016; 8(23): 11851–11861.
31. Sharkeev Y, Sedelnikova M, Tolkacheva T, et al. Micro-Arc Zn- and Ag-containing coatings for implants with complex porous architecture obtained by 3D printing method from titanium alloy. *Travmatologiya Ortopediya Rossii* 2020; 26(2): 109–119.
32. Li Y, Li L, Ma Y, et al. 3D-printed titanium cage with PVA-vancomycin coating prevents surgical site infections (SSIs). *Macromol Biosci* 2020; 20(3): 1900394.
33. Liu H, Wang C, Li C, et al. A functional chitosan-based hydrogel as a wound dressing and drug delivery system in the treatment of wound healing. *RSC Adv* 2018; 8(14): 7533–7549.
34. Bai H, Cui Y, Wang C, et al. 3D printed porous biomimetic composition sustained release zoledronate to promote osteointegration of osteoporotic defects. *Mater Des* 2020; 189: 108513.
35. Tang B, Wang J, Xu S, et al. Application of anisotropic silver nanoparticles: multifunctionalization of wool fabric. *J Colloid Interface Sci* 2011; 356(2): 513–518.
36. Wu M, Ma B, Pan T, et al. Silver-nanoparticle-colored cotton fabrics with tunable colors and durable antibacterial and self-healing superhydrophobic properties. *Adv Funct Mater* 2016; 26(4): 569–576.
37. Li Z, Wang C, Li C, et al. What we have achieved in the design of 3D printed metal implants for application in orthopedics? Personal experience and review. *Rapid Prototyp J* 2018; 24(8): 1365–1379.
38. Chen Z, Yan X, Yin S, et al. Influence of the pore size and porosity of selective laser melted Ti6Al4V ELI porous scaffold on cell proliferation, osteogenesis and bone ingrowth. *Mater Sci Eng C Mater Biol Appl* 2020; 106: 110289.
39. Raphel J, Holodniy M, Goodman SB, et al. Multifunctional coatings to simultaneously promote osseointegration and prevent infection of orthopaedic implants. *Biomaterials* 2016; 84: 301−314.
40. Kumar A, Nune KC and Misra RDK. Design and biological functionality of a novel hybrid Ti-6Al-4V/hydrogel system for reconstruction of bone defects. *J Tissue Eng Regen Med* 2018; 12(4): 1133–1144.
41. Li J, Li L, Zhou J, et al. 3D printed dual-functional biomaterial with self-assembly micro-nano surface and enriched nano argentum for antibalctorial and bone regeneration. *Appl Mater Today* 2019; 17: 206–215.
42. Rashdan NA, Sim AM, Cui L, et al. Osteocalcin regulates arterial calcification via altered wnt signaling and glucose metabolism. *J Bone Miner Res* 2020; 35(2): 357–367.
43. Sivashanmugam A, Charoenlarp P, Deepthi S, et al. Injectable shear-thinning CaSO(4)/FGF-18-incorporated chitin-PLGA hydrogel enhances bone regeneration in mice cranial bone defect model. *ACS Appl Mater Interfaces* 2017; 9(49): 42639–42652.
44. Ho SS, Vollmer NL, Refaat MI, et al. Bone morphogenetic protein-2 promotes human mesenchymal stem cell survival and resultant bone formation when entrapped in photocrosslinked alginate hydrogels. *Adv Healthcare Mater* 2016; 5(19): 2501–2509.
45. Carlisle EM. Silicon: a possible factor in bone calcification. *Science* 1970; 167(3916): 279–280.
46. Wang C, Lin K, Chang J, et al. Osteogenesis and angiogenesis induced by porous β-CaSiO(3)/PDLGA composite scaffold via activation of AMPK/ERK1/2 and PI3K/Akt pathways. *Biomaterials* 2013; 34(1): 64–77.
47. Sun W, Zhou Y, Zhang X, et al. Injectable nano-structured silicon-containing hydroxyapatite microspheres with enhanced osteogenic differentiation and angiogenic factor expression. *Ceram Int* 2018; 44(16): 20457–20464.
48. Yang Y, Yang S, Wang Y, et al. Anti-infective efficacy, cytocompatibility and biocompatibility of a 3D-printed osteoconductive composite scaffold functionalized with quaternized chitosan. *Acta Biomater* 2016; 46: 112–128.
49. Yang Y, Chu L, Yang S, et al. Dual-functional 3D-printed composite scaffold for inhibiting bacterial infection and promoting bone regeneration in infected bone defect models. *Acta Biomater* 2018; 79: 265–275.
50. Liu X, Bao C, Xu HHK, et al. Osteoprotegerin gene-modified BMSCs with hydroxyapatite scaffold for treating critical-sized mandibular defects in ovariectomized osteoporotic rats. *Acta Biomater* 2016; 42: 378–388.
51. Romanò CL, Manzi G, Logoluso N, et al. Value of debridement and irrigation for the treatment of peri-prosthetic infections. A systematic review. *HIP Int* 2012; 22(Suppl 8): S19–S24.
52. Yao QQ, Zhou J, Jiang CZ, et al. Mechanical and in vitro antibacterial properties of a porous Ti-6Al-4V scaffold combined with vancomycin-loaded polymethyl methacrylate by three-dimensional printing. *J Biomater Tissue Eng* 2018; 8(5): 740–749.
53. Penn-Barwell JG, Murray CK and Wenke JC. Local antibiotic delivery by a bioabsorbable gel is superior to PMMA bead depot in reducing infection in an open fracture model. *J Orthop Trauma* 2014; 28(6): 370–375.
54. Arcos D and Vallet-Regi M. Bioceramics for drug delivery. *Acta Mater* 2013; 61(3): 890–911.

55. Campoccia D, Montanaro L, Speziale P, et al. Antibiotic-loaded biomaterials and the risks for the spread of antibiotic resistance following their prophylactic and therapeutic clinical use. *Biomaterials* 2010; 31(25): 6363–6377.
56. Chen WL, Chang WN, Chen YS, et al. Acute community-acquired osteoarticular infections in children: high incidence of concomitant bone and joint involvement. *J Microbiol Immunol Infect = Wei mian yu gan ran za zhi*. 2010; 43(4): 332–338.
57. Tong SY, Davis JS, Eichenberger E, et al. Staphylococcus aureus infections: epidemiology, pathophysiology, clinical manifestations, and management. *Clin Microbiol Rev* 2015; 28(3): 603–661.
58. Rodríguez-Pardo D, Pigrau C, Lora-Tamayo J, et al. Gram-negative prosthetic joint infection: outcome of a debridement, antibiotics and implant retention approach. A large multicentre study. *Clin Microbiol Infect Off Public Eur Soc Clin Microbiol Infect Dis* 2014; 20(11): O911−O919.
59. Lamagni T, Elgohari S and Harrington P. Trends in surgical site infections following orthopaedic surgery. *Curr Opin Infect Dis* 2015; 28(2): 125–132.
60. Anisha BS, Biswas R, Chennazhi KP, et al. Chitosan-hyaluronic acid/nano silver composite sponges for drug resistant bacteria infected diabetic wounds. *Int J Biol Macromol* 2013; 62: 310–320.
61. Zhang S, Guo Y, Dong Y, et al. A novel nanosilver/nano-silica hydrogel for bone regeneration in infected bone defects. *ACS Appl Mater Interfaces* 2016; 8(21): 13242–13250.
62. Huang Q, Elkhooly TA, Liu X, et al. Effects of hierarchical micro/nano-topographies on the morphology, proliferation and differentiation of osteoblast-like cells. *Colloids Surf B Biointerfaces* 2016; 145: 37–45.
63. He X, Zhang X, Li J, et al. Titanium-based implant comprising a porous microstructure assembled with nanoleaves and controllable silicon-ion release for enhanced osseointegration. *J Mater Chem B* 2018; 6(31): 5100–5114.
64. Wang X, Gao L, Han Y, et al. Silicon-enhanced adipogenesis and angiogenesis for vascularized adipose tissue engineering. *Adv Sci* 2018; 5(11): 1800776.